Earthquake Source Spectra Estimates Vary Widely for Two Ridgecrest Aftershocks Because of Differences in Attenuation Corrections

Peter M. Shearer[*1] , Ian Vandevert[1] , Wenyuan Fan[1] , Rachel E. Abercrombie[2] , Dino Bindi[3] , Giovanna Calderoni[4] , Xiaowei Chen[5] , William Ellsworth[6] , Rebecca Harrington[7] , Yihe Huang[8] , Trey Knudson[6] , Meggy Roßbach[7] , Claudio Satriano[9] , Mariano Supino[4] , Daniel T. Trugman[10] , Hongfeng Yang[11] , and Jiewen Zhang[11]

ABSTRACT

Differences in stress-drop estimates among groups of scientists for the same earthquakes suggest disagreement in the shape of the source spectra that are used to measure corner frequency. A critical step in characterizing source spectra involves applying empirical corrections for site effects and the loss of high-frequency energy that occurs along the source–receiver path. As part of the Ridgecrest stress-drop validation study, we compare path-corrected source spectra among different methods for two nearly collocated M 3 earthquakes and investigate whether systematic differences in the applied path corrections are affecting corner-frequency estimates. We find substantial disagreements in the path corrections, which are well approximated with a simple exponential function related to the strong ground motion parameter κ. These κ differences are strongly correlated with corner-frequency estimates for path-corrected spectra, suggesting they are a large source of systematic differences in corner frequency (and inferred stress drop) among the methods, reflecting varying trade-offs between the source and path contributions to observed spectra. Because each method presumably fits the data it uses sufficiently well, these results indicate the limitations of existing purely empirical techniques to estimating path corrections and the need for new approaches.

KEY POINTS

- Earthquake stress-drop estimates derived from source spectra disagree widely for different groups and methods.
- Variations in corrections for seismic attenuation are a large contributor to uncertainties in stress drop.
- New approaches are needed to characterize the loss of high-frequency energy between source and receiver.

Supplemental Material

1. Scripps Institution of Oceanography, UC San Diego, La Jolla, California, U.S.A., https://orcid.org/0000-0002-2992-7630 (PMS); https://orcid.org/0000-0001-9560-4787 (IV); https://orcid.org/0000-0002-2983-8240 (WF); 2. Department of Earth and Environment, Boston University, Boston, Massachusetts, U.S.A., https://orcid.org/0000-0003-4515-5420 (REA); 3. German Research Centre for Geoscience GFZ, Potsdam, Germany, https://orcid.org/0000-0002-8619-2220 (DB); 4. Istituto Nazionale di Geofisica e Vulcanologia, Osservatorio Nazionale Terremoti, Rome, Italy, https://orcid.org/0000-0002-3712-4432 (GC); https://orcid.org/0000-0002-7222-9344 (MS); 5. Department of Geology and Geophysics, Texas A & M University, College Station, Texas, U.S.A., https://orcid.org/0000-0001-6362-3297 (XC); 6. Department of Geophysics, Stanford University, Stanford, California, U.S.A., https://orcid.org/0000-0001-8378-4979 (WE); https://orcid.org/0009-0007-0350-5732 (TK); 7. Institute of Geology, Mineralogy, and Geophysics, Ruhr University Bochum, Bochum, Germany, https://orcid.org/0000-0002-3538-8020 (RH); https://orcid.org/0009-0005-0732-9559 (MR); 8. Department of Earth and Environmental Sciences, University of Michigan, Ann Arbor, Michigan, U.S.A., https://orcid.org/0000-0001-5270-9378 (YH); 9. Institut de physique du globe de Paris, CNRS, Université Paris Cité, Paris, France, https://orcid.org/0000-0002-3039-2530 (CS); 10. Nevada Seismological Laboratory, University of Nevada, Reno, Nevada, U.S.A., https://orcid.org/0000-0002-9296-4223 (DTT); 11. Department of Earth and Environmental Sciences, The Chinese University of Hong Kong, Hong Kong S.A.R., China, https://orcid.org/0000-0002-5925-6487 (HY); https://orcid.org/0000-0001-8130-9453 (JZ)

*Corresponding author: pshearer@ucsd.edu

INTRODUCTION

The large scatter in spectral stress-drop estimates obtained by different researchers for the same earthquakes (e.g., Abercrombie, 2021; Pennington *et al.*, 2021) motivated development of the Ridgecrest stress drop validation study Baltay *et al.* (2024), which is the subject of this special issue (e.g., Abercrombie, Baltay, *et al.*, 2024). One of the study goals is to compare results from different analysis methods to gain an understanding of the origins of the observed differences. Although there are many factors that can affect stress-drop measurements, one of the most important factors is the correction to the observed *P*- or *S*-wave spectra that

accounts for attenuation along the source–receiver path. Indeed, it has long been recognized that there is a trade-off between the fall-off in high-frequency radiation from the earthquake source and attenuation along the path (e.g., Hanks and McGuire, 1981; Frankel, 1982; Hanks, 1982; Anderson and Hough, 1984; Anderson, 1986).

The source spectrum is typically modeled following Brune (1970), in which the displacement amplitude spectrum has the form

$$A(f) = \frac{\Omega_0}{[1 + (f/f_c)^{\gamma n}]^{1/\gamma}}, \tag{1}$$

in which f is frequency; Ω_0 is the low-frequency limit; f_c is the corner frequency; n is the high-frequency fall-off rate; and γ controls the sharpness of the corner ($\gamma = 1$, $n = 2$ for the standard Brune model).

The strong ground motion community often characterizes the observed high-frequency fall-off of the acceleration spectrum as

$$A(f) = A_0 e^{-\pi \kappa f}, \tag{2}$$

in which f is frequency; and the parameter κ includes both source and path effects. For the widely used ω-square source model (e.g., Aki, 1967; Brune, 1970), $n = 2$ in equation (1) and the acceleration spectrum is flat above the corner frequency and κ can be related to the integrated effect of attenuation along the ray path, that is,

$$\kappa = \int_{\text{path}} \frac{dt}{Q(\mathbf{r})}, \tag{3}$$

in which Q is the attenuation quality factor; t is time; and $\mathbf{r}$ is position. In this case, κ is identical to the parameter t^* that is often also used to describe integrated attenuation. However, in general, κ may include contributions from both the source (deviations from the Brune $n = 2$ model) and the path (Q).

In general, κ grows with distance from a given earthquake because longer paths suffer more attenuation. However, there is a path-independent part of κ, termed κ_0, which represents either deviations from the Brune model or attenuation in the shallow crust immediately below the station. It is difficult to separate the source and near-surface attenuation contributions to κ_0 purely from observations. However, assuming a Brune source model, then κ_0 observations indicate strong near-surface attenuation (e.g., Frankel, 1982; Anderson and Hough, 1984), a result supported by borehole studies of shallow attenuation, even at hard-rock sites (e.g., Aster and Shearer, 1991; Abercrombie and Leary, 1993; Abercrombie, 1997).

Because of the difficulty in measuring path attenuation directly, a common approach in spectral stress-drop studies is to apply purely empirical methods to estimate the path correction. The empirical Green's function (EGF) method (e.g., Mueller, 1985; Mori and Frankel, 1990) uses one or more small earthquakes near the target earthquake of interest as calibration (EGF) events to correct the target event spectrum. In its ideal form, small earthquakes have a perfectly flat spectrum and are close enough to the target event to have the same path correction, and no additional assumptions about the source are necessary. However, for real data sets the EGF events are not small enough to have completely flat spectra and thus various approaches have been developed to simultaneously fit the spectra of large and small events. As shown in Shearer et al. (2019), different EGF analysis methods may produce contradictory results, that is, obtaining a good fit to the data using one approach and/or assumptions about the source may not yield the same effective path correction as another approach that also fits the data well. Because different path corrections are related to variations in the amount of high-frequency energy in the corrected source spectra, these variations will lead to differences in the average stress drops among different studies.

Large variations in corner frequency and stress drop are indeed observed among submissions to the Ridgecrest stress-drop validation study Abercrombie, Baltay, et al. (2024). Our goal here is to investigate whether different path corrections are contributing to these variations by comparing results for two specific Ridgecrest earthquakes recorded at 12 nearby stations. We find that different approaches obtain different path corrections, which can be approximated as differences in the path contribution to κ, and that this can explain much of the variations in average stress drop among different groups.

TARGET EARTHQUAKES AND STATIONS

To simplify comparisons among the different methods, we focus on two nearly collocated Ridgecrest aftershocks,

1. 7 July 2019 03:23:26.8, M 3.30, 35.8733°, −117.7182°, 7.78 km, ID = 38471103; and
2. 8 July 2019 05:02:10.5, M 3.13, 35.8758°, −117.7198°, 7.75 km, ID = 38483215.

Event information is from the relocated catalog of Trugman (2020). These events are included in the selected subsets identified in the Ridgecrest validation exercise for more detailed study. Because the event epicenters are only about 300 m apart, their path corrections to individual stations should be very similar, which provides a good check on the internal consistency of path correction estimates within results from a single group. For simplicity, we limit our comparison to 12 nearby stations for the P waves and 9 nearby stations for the S waves (see Fig. 1). The P-wave stations are: PB B916 EHZ, PB B917 EHZ, PB B918 EHZ, CI CCA HHZ, CI CCC HHZ, CI CGO HHZ, CI CLC HHZ, CI CWC HHZ, CI DAW HHZ, CI DTP HHZ, CI JRC2 HHZ, and CI ISA HHZ. The S-wave stations are: PB B916 EH2, PB B917 EH1, PB B921 EH1 and EH2, CI CWC HHE, CI ISA HHN, CI JRC2 HHE and HHN, CI LRL HHE, CI SRT HHN, and CI TEH HHE and HHN.
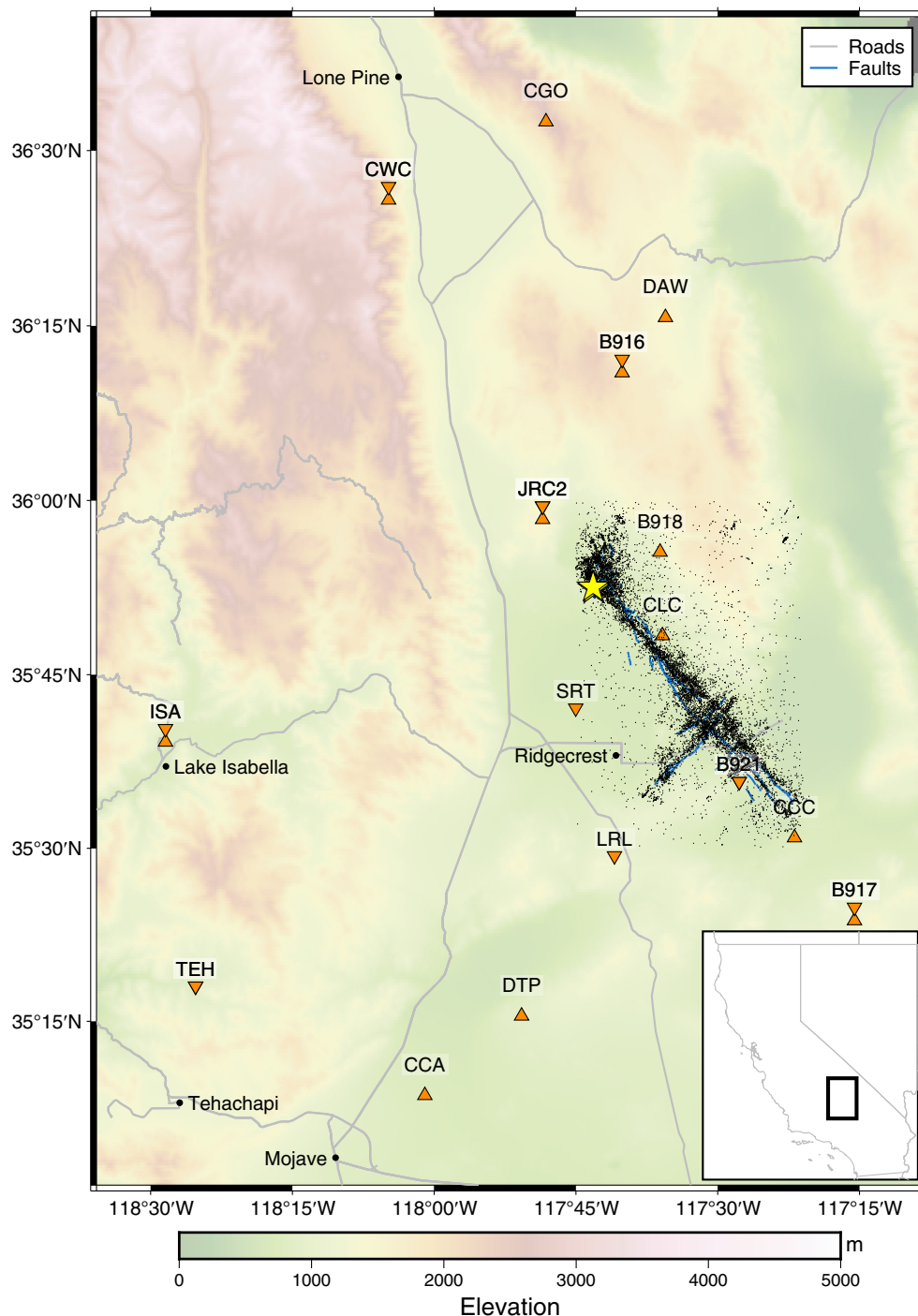
Figure 1. A map showing the locations of the two target earthquakes (nearly overlapping yellow stars) and the stations used in this analysis (triangles for *P* waves, inverted triangles for *S* waves). Aftershocks of the 4 July M 6.4 and 5 July M 7.1 Ridgecrest mainshocks are shown as gray dots. Roads and rivers are also shown. The color version of this figure is available only in the electronic edition.

spectrum that they used to estimate source corner frequencies. Because these group methods and results are described elsewhere in this special issue Abercrombie, Baltay, *et al.* (2024), we do not include many details here (the Appendix has a brief summary of each method).

Each observed spectrum can be modeled as a product of event, path, and station terms,

$$a(f) = e(f)p(f)s(f), \quad (4)$$

in which $e(f)$ is the event (source) spectrum; $p(f)$ is the path term (which accounts for geometrical spreading and attenuation); and $s(f)$ is the station term (which includes local site effects and the instrument response if $a(f)$ is an uncorrected raw spectrum). This becomes a sum in the log domain,

$$\log a(f) = \log e(f) + \log p(f) + \log s(f), \quad (5)$$

$$A(f) = E(f) + P(f) + S(f), \quad (6)$$

in which capital letters are used in this section to designate the log spectra.

The goal in source spectral studies is to remove the effects of the path and station terms on the observed spectra to obtain estimates of the source spectra, which is typically approximated as constant over the different recording stations. Here, we will name the combined path and station term the total path correction (TPC). Note that the TPC contains the effects of attenuation along ray path and represents the complete source-to-receiver Green's function, including any station- or site-specific effects, such as strong attenuation and/or resonance in near-surface layers.

DATA ANALYSIS

Our study involves a comparison of *P* and *S* spectra processed by 12 different groups for these two test earthquakes. In each case, we asked the group to submit both the original raw spectrum for each station and the final path- and site-corrected

As explained in Abercrombie, Baltay, *et al.* (2024), the methods fall into a few general categories. We include brief descriptions here to clarify the meaning of the TPC that we analyze for each group.

Generalized inversion and spectral decomposition

Models BINDI, CHEN, TRUG, VSF-P, VSF-S, ZHANG-P, and ZHANG-S are examples of generalized inversion and spectral decomposition techniques. These are generally applied to large data sets with many sources and receivers and solve for best-fitting source, station, and path terms. In this case we can write

$$A_{ij}(f) = E_i(f) + P_{ij}(f) + S_j(f), \qquad (7)$$

in which $A_{ij}(f)$ is the observed log spectrum from event i to station j; and P_{ij} is the path term. The path term can be discretized as a function of source–receiver travel time (e.g., Shearer *et al.*, 2006) or, using a nonparametric approach can be described in terms of a depth-varying attenuation model (e.g., Bindi *et al.*, 2023a). This system can be solved for a best-fitting set of event, path, and station terms but has no unique solution in that a constant spectrum could be added to one of the terms and subtracted from a different term without changing their sum. To address this ambiguity, a correction spectrum, termed here the empirical correction spectrum (ECS), is computed based on some model of the expected shape of the source spectrum. The final source spectral estimate is then given by

$$E_{\text{corrected}}(f) = E(f) - \text{ECS}(f), \qquad (8)$$

in which $E(f)$ is the event log spectrum from the original spectral decomposition. Different groups estimate the ECS in different ways, and this is likely a major source of variations in their final results. For example, Trugman (2020) finds the best-fitting ECS to a Brune source model in which stress-drop scales linearly with moment, whereas Vandevert *et al.* (2024) compute the ECS by assuming that small earthquakes (close to a reference magnitude) have a specific fixed corner frequency. In addition, note that some analyses compute a single ECS for the entire data set whereas others allow it to vary spatially.

Our study examines the final TPC-corrected spectrum for each station, which is given by

$$A_{ij}(\text{TPC corrected}) = A_{ij} - P_{ij} - S_j - \text{ECS}. \qquad (9)$$

Q- and κ-based fitting methods

These methods vary considerably in their details but typically involve assuming that the path term relates to an attenuation model that can be described in terms of Q or κ. This differs from many spectral decomposition approaches, in which the path term is free to vary and is not tied to an exponential function or a physical attenuation model. However, the methods in

this section often also apply an empirical station-specific correction (i.e., a site term) in addition to the path term. Examples in this study include CALD-S, which solves for κ-values; ROSS-P and ROSS-S, which solve for best-fitting values of source high-frequency fall-off (n) and Q for the entire data set; SSPEC, which fits each spectrum for κ while assuming $n = 2$; SPAR, which fits each spectrum for best-fitting n- and Q-values; and KNUD, which computes frequency-dependent attenuation functions that are tied together using an assumed frequency-independent $Q = 100$ in the last 10 km to the station. Note that KNUD computes spectra using a band-pass filtering method rather than a Fourier transform approach.

Spectral ratio methods

Models ABER and HUANG use a spectral ratio approach. These methods identify a set of smaller earthquakes near each target event that are termed EGF events. Note that ABER and HUANG apply different distance cutoffs from the target event in selecting the EGF events; ABER uses events within 2 km, whereas HUANG uses events within 250 m. However, in both cases they are assumed to be close enough to the target event that they share the same total path correction, such that the observed spectral ratio between the target and EGF observed spectra is equal to the ratio of their source spectra,

$$A_{\text{targ}} - A_{\text{EGF}} = E_{\text{targ}} - E_{\text{EGF}}, \qquad (10)$$

in which the ratio is expressed as a difference in the log spectral domain. Assuming a model for the shape of the expected source spectrum, best-fitting values for the target and EGF event corner frequencies (f_c^{targ} and f_c^{EGF}) can then be computed from this ratio, although sometimes the ratios are stacked over different stations and/or EGF events first.

Because the spectral ratio method does not explicitly compute a TPC or a final corrected source spectrum, we use the method explained in Shearer *et al.* (2019) to estimate the underlying TPC. Note f_c^{targ} and f_c^{EGF} predict model spectra M_{targ} and M_{EGF} that will differ from the observed spectra by the TPC,

$$A_{\text{targ}} - M_{\text{targ}} = \text{TPC} + r_{\text{targ}}, \qquad (11)$$

$$A_{\text{EGF}} - M_{\text{EGF}} = \text{TPC} + r_{\text{EGF}}, \qquad (12)$$

in which r_{targ} and r_{EGF} are the residuals to the fits to the target and EGF spectra, respectively. We can then estimate the TPC by averaging the residuals:

$$\text{TPC} = \frac{(A_{\text{targ}} - M_{\text{targ}}) + (A_{\text{EGF}} - M_{\text{EGF}})}{2}. \qquad (13)$$

This is the same as equation (12) in Shearer *et al.* (2019) (which has a typo—the division by 2 is missing).
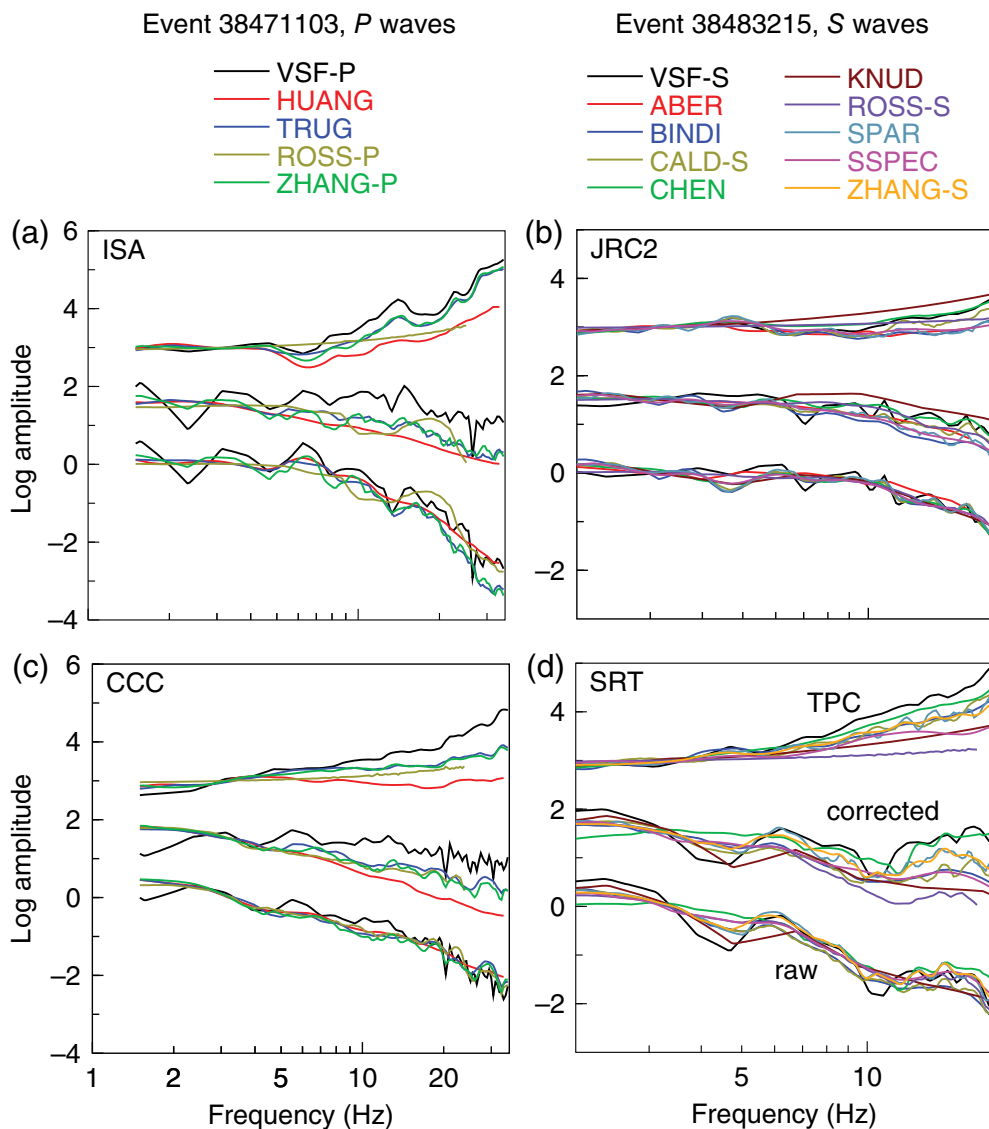
Figure 2. Examples of *P*- and *S*-wave results from different contributing groups at selected stations. Colors are used to indicate spectra for each group. Within each panel, the raw spectra, the total path corrected spectra, and the total path correction (TPC) are shown from bottom to top, with 1.5-unit amplitude offsets applied for clarity. (a,c) *P*-wave spectra for the first target event (M 3.30, cuspid 38471103); (b,d) *S*-wave spectra for the second target event (M 3.13, cuspid 38483215). The color version of this figure is available only in the electronic edition.
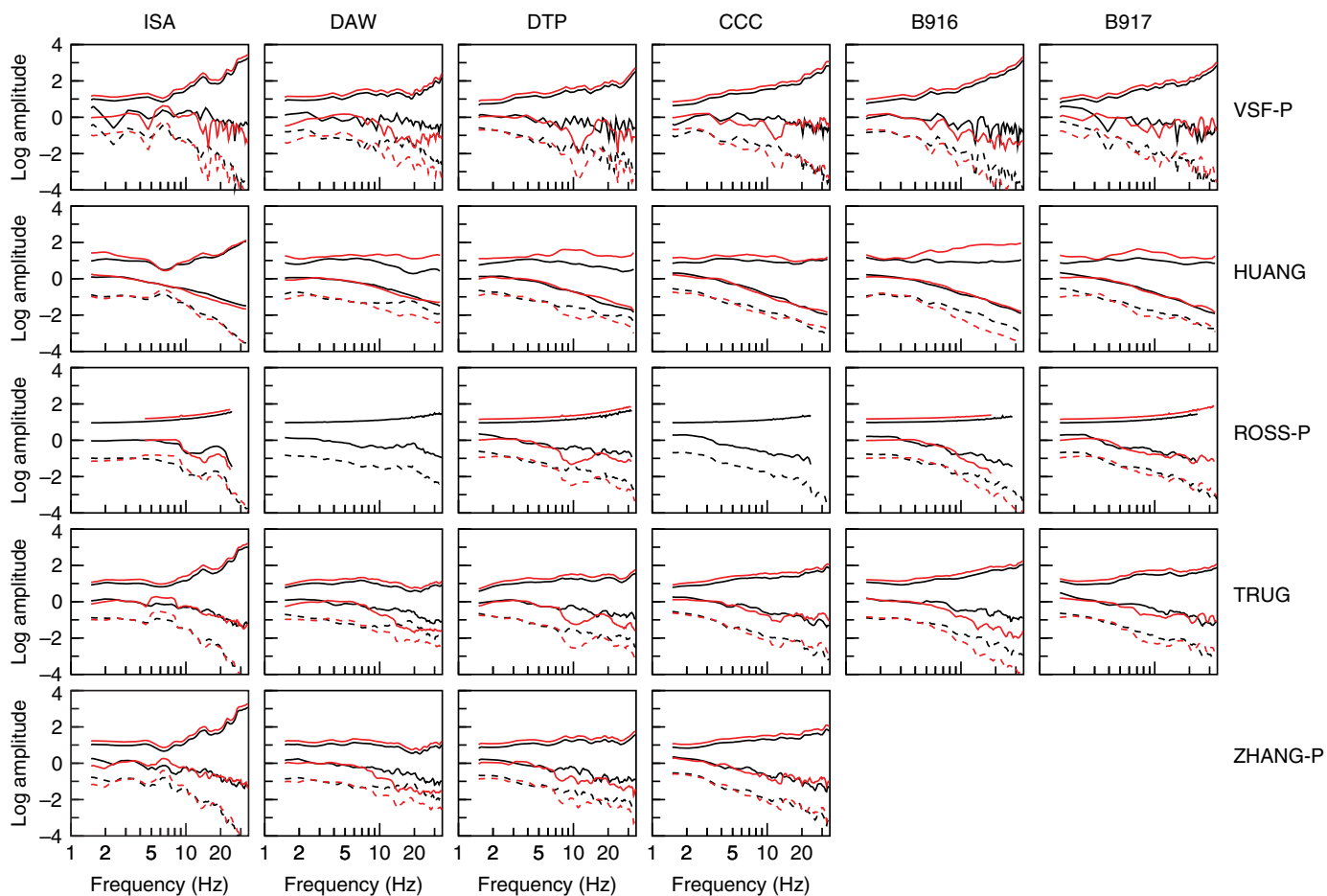
RESULTS

Many comparisons are possible among the results obtained by different groups for the Ridgecrest validation study (e.g., Abercrombie, Baltay, *et al.*, 2024; Baltay and Abercrombie, 2024; Cochran *et al.*, 2024). Our goal here is to focus on the TPC corrections applied to the observed spectra and assess how differences in these corrections may be contributing to variations in corner-frequency estimates. To simplify the analysis, we examine data from only two target events as recorded by a small number of nearby stations, even though in many cases the TPC terms are computed using a much larger data set. Note that we do not attempt to assess why different methods obtain different path corrections, only to

measure these differences and check how they relate to corner-frequency estimates. Accordingly, we do not examine differences in low-frequency levels (proportional to moment); we compare spectral shapes by normalizing results to the same low-frequency spectral amplitude.

Different groups use different frequency points, owing to variations in the time-series window length, spectral estimation method, or later resampling. This complicates our processing and comparisons, so we first resample all the spectra to 200 frequency points at uniform intervals in log frequency using a linear interpolation between points. In doing so, we do not extrapolate any results beyond the frequency range at which they were originally submitted. We correct velocity spectra to displacement as necessary.

Example spectra are shown in Figure 2. The TPC (shown as the upper set of curves in each panel) is simply the difference between the corrected log spectra and the raw log spectra. Two groups (ABER and HUANG) use spectral ratio methods that do not explicitly compute path corrections. In these cases, we estimate the effective TPC using equation (13) and the values of f_c^{targ} and f_c^{EGF} derived from the spectral ratio. We then use this TPC to generate corrected source spectra to plot in the figures. Notice that the raw spectra show some variations among the groups, presumably owing to differences in the time-domain window applied and the choice of spectral estimation method, but the raw spectra show better agreement than the corrected spectra. In many respects, our TPC analysis would have been easier to interpret if we had asked each group to begin with the same set of raw spectra. However, as a practical matter it was far easier to compare results that were already being prepared as part of the larger Ridgecrest stress-drop validation exercise. Because in the log domain the TPC spectra are simply the corrected spectra

Figure 3. *P*-wave results from different contributing groups at six selected stations (labeled at top of columns). The first target event (M 3.30, cuspid 38471103) is plotted in black, the second event (M 3.13, cuspid 38483215) is plotted in red. Within each panel, the raw spectra (dashed lines), the TPC-corrected spectra, and the TPC are shown from bottom to top, with a one unit amplitude offset applied for clarity. An additional 0.2 *y*-offset is applied to the second event TPC curves to avoid completely overlapping the first event curves. The color version of this figure is available only in the electronic edition.

minus the raw spectra, it is not surprising that the TPC and corrected spectra exhibit similar amounts of scatter, given the approximate agreement in the raw spectra.

To see the variations among the different groups more clearly, we plot the raw submitted spectra, the corrected spectra, and their differences at six selected stations as shown in Figure 3 for *P* waves and Figure 4 for *S* waves. These plots reveal both similarities and variations in the results among the different groups. The VSF-P and VSF-S raw and corrected spectra are rougher than those of the other groups, a result of computing spectra using a simple Hann taper rather than a multitaper method that involves spectral smoothing. Because the two target events are only 300 m apart, it is likely that the true total path correction to each station will be nearly the same for both events (implying that differences in the spectra observed at the same station are mainly caused by source rather than path differences). This is generally the case for most of the methods but differences between the TPC spectra for the two events are seen for some methods, most noticeably for HUANG and CALD-S, but also to some extent for ABER, SPAR, and SSPEC.

There is some degree of correlation among the method results at individual stations. For example, the *S*-wave TPC for station SRT is generally stronger than that for station JRC2, despite the similar distance of these stations from the events. TPC curves resulting from different methods also show

similar patterns of oscillations with frequencies for individual stations. For example, the *P*-wave TPC for station ISA is observed to decrease and increase again between 5 and 10 Hz by VSF-P, HUANG, TRUG, and ZHANG-P. There is strong correlation in the TPC over different stations for the same method, that is, methods that produce strong TPC for one station tend to produce strong TPC for other stations. For example, among the *P*-wave models, VSF-P has strong corrections at all stations and ROSS-P has relatively weak corrections at all stations.

To make these method differences more apparent, we average the corrected log spectra and the TPC log spectra over all available stations (among the target stations only) for each group. These results are shown in Figures 5 for *P* waves and 6 for *S* waves. The stacks of the corrected log spectra represent a first-order estimate of the true source spectrum
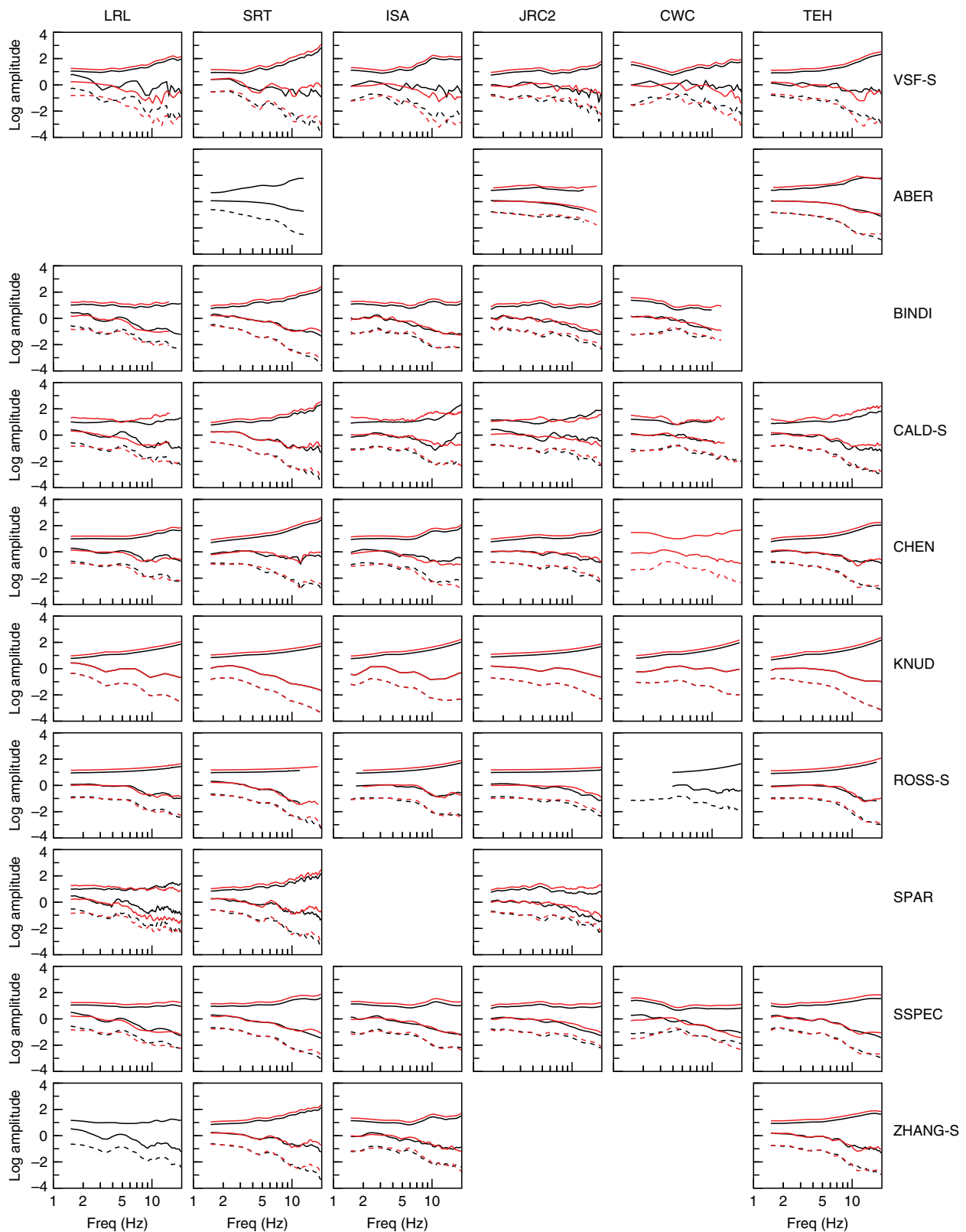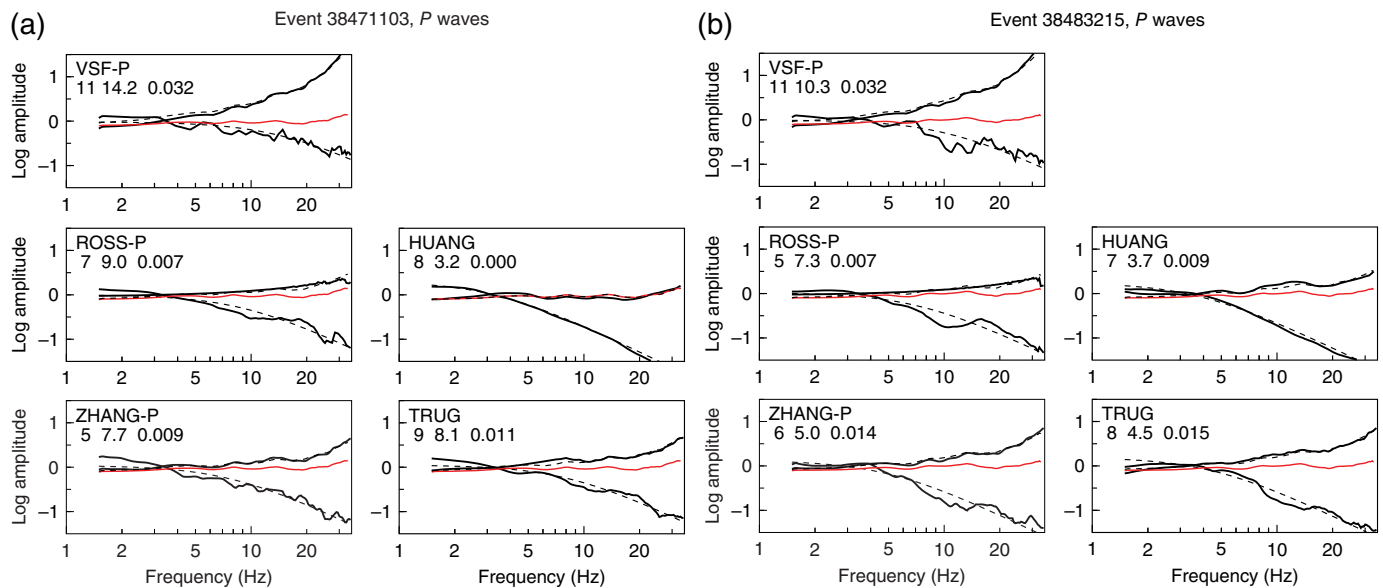
Figure 4. *S*-wave results from different contributing groups at six selected stations (labeled at top of columns). The first target event (M 3.30, cuspid 38471103) is plotted in black, the second event (M 3.13, cuspid 38483215) is plotted in red. Within each panel, the raw spectra (dashed lines), the TPC-corrected spectra, and the TPC are shown from bottom to top, with a one unit amplitude offset applied for clarity. An additional 0.2 *y*-offset is applied to the second event TPC curves to avoid completely overlapping the first event curves. The color version of this figure is available only in the electronic edition.

(a) Event 38471103, P waves
(b) Event 38483215, P waves

Figure 5. Stacks over available stations of the corrected log *P*-wave spectra (lower black curves) and the TPC corrections (upper black curves) for target (a) event 1 and (b) event 2. The number of stations contributing to the stack is indicated by the first number below the group label. The lower dashed lines show the Brune-model fit to the corrected spectra (corner frequency in Hertz indicated by the second number below the group label). The upper dashed lines show the fit to the TPC results provided by the model described in the text, characterized by a constant spectrum (red line) and a group-specific value of $\Delta\kappa$ (the number in seconds following the corner frequency). The color version of this figure is available only in the electronic edition.

for each event, and large differences are apparent among the different methods. For example, among the *S*-wave models, VSF-S has much more high-frequency energy in its corrected spectra stack than SSPEC, consistent with the fact that VSF-S TPC corrections are adding more high-frequency energy to the raw spectra than the SSPEC TPC corrections. To quantify these differences, we compute corner frequencies (f_c) for the corrected log spectra stacks assuming a Brune model with a high-frequency falloff rate of f^{-2}; these fits are plotted as the dashed lines in the figure panels with the corresponding f_c-values labeled.

For each event and wave type, we experiment with fitting the TPC log spectra over all groups with a function of the form

$$\mathrm{TPC}_i(f) = \mathrm{TPC}_0(f) + \log 10[e^{\pi\Delta\kappa_i f}], \tag{14}$$

in which $\mathrm{TPC}_i(f)$ is the TPC spectrum for group i; $\mathrm{TPC}_0(f)$ is a single spectrum common to all groups; and $\Delta\kappa_i$ is a group-specific value that accounts for differences in the path part of κ (see equation 2) among the groups and controls the relative amount of high-frequency radiation that is added back into the raw spectra to create the corrected spectra. In the figures, $\mathrm{TPC}_0(f)$ is shown in red, the $\Delta\kappa_i$-values (in seconds) are indicated below the group labels, and the fits obtained with equation (14) shown as the dashed lines.

In general, we obtain good fits to the TPC station stacks for each group with this simple model. The $\Delta\kappa_i$-values describe overall attenuation differences among the methods, which are related to the assumed strength of high-frequency radiation from the earthquake source. The $\mathrm{TPC}_0(f)$ curves are bumpier than the smooth predictions of the κ models and likely reflect station-specific site effects (e.g., resonances in near-surface layers), seen by all the groups, that have not been completely averaged out by the station stacks.
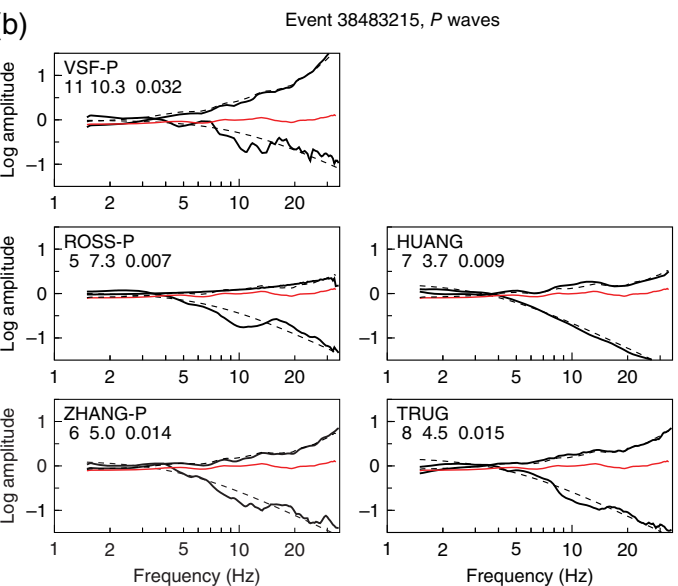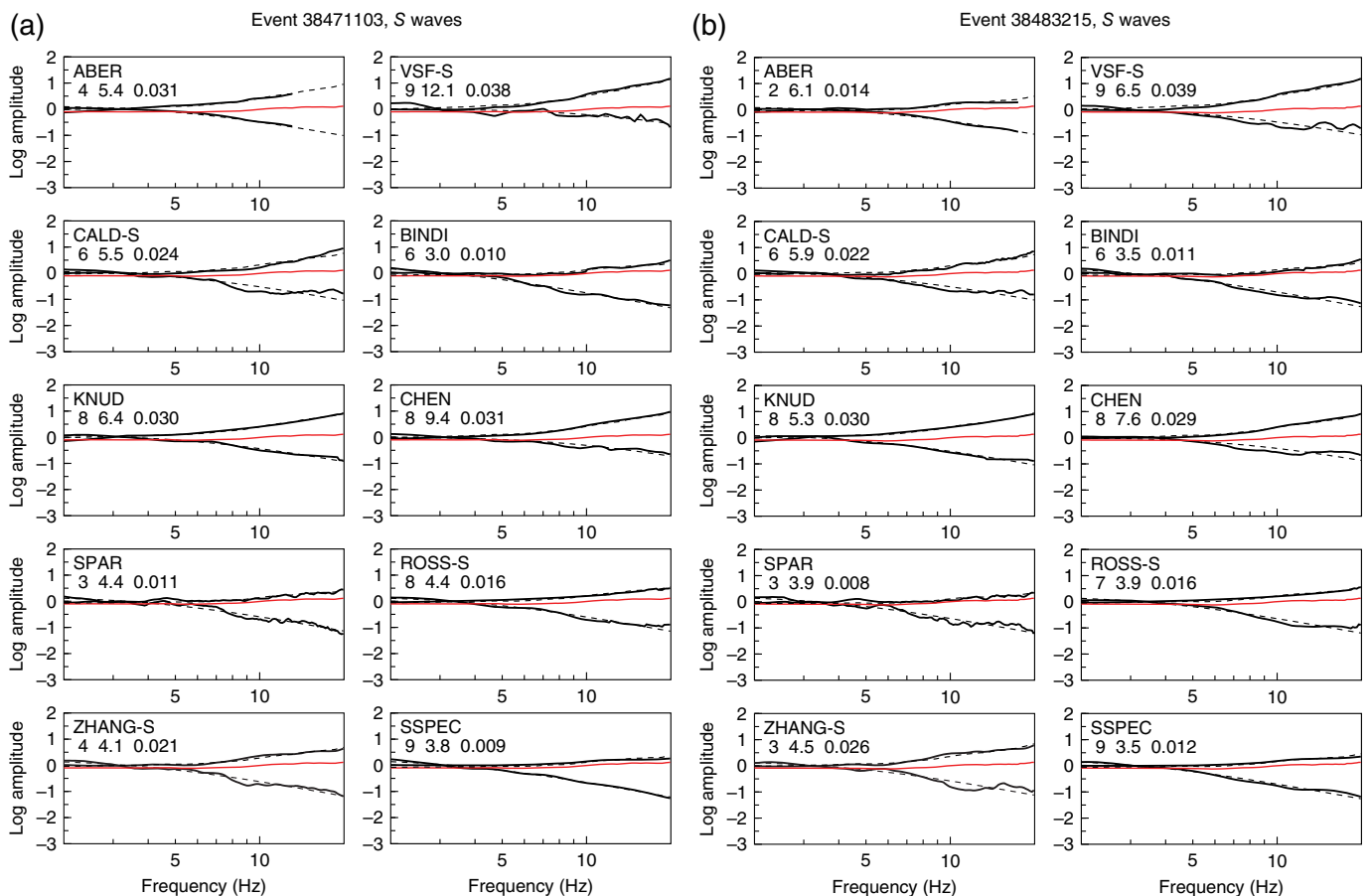
DISCUSSION AND CONCLUSIONS

Variations in observed *P*- and *S*-wave spectra arise from both source and path effects, and obtaining an accurate and unbiased estimate of the true earthquake source spectrum, averaged over the focal sphere, is a challenging task. Both source complexity (e.g., directivity, subevents, etc.) and path complexity (e.g., fault zone structure and 3D attenuation structure) contribute to misfits between real data and simplified theoretical models. Our focus here is on a subset of this problem, examining the consistency of the corrections used by different methods to account for along-path attenuation for identical source–receiver pairs.

As discussed earlier because the two target events are only about 300 m apart, we expect each group's total path corrections to be nearly identical for the two events at the same stations and this is observed for most groups in Figures 3 and 4. However, HUANG and CALD-S have distinctly different TPC spectra for the two events, and ABER, SPAR, and SSPEC also have some variations. This highlights a potential weakness of methods that treat each target event individually without requiring similarity in path corrections for nearby events. Both ABER and HUANG use spectral ratios and the better agreement in the TPC corrections for ABER likely results from averaging over a larger number of EGF calibration events.
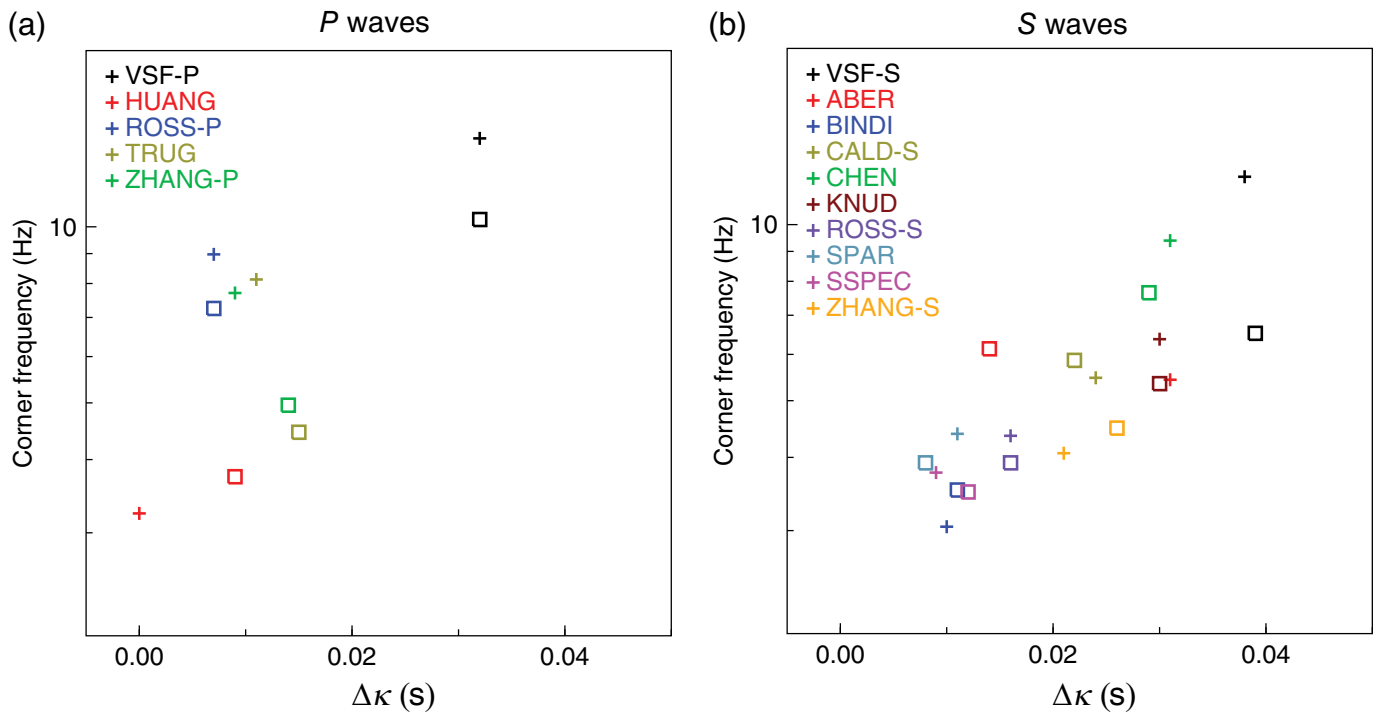
Figure 6. Stacks over available stations of the corrected log *S*-wave spectra (lower black curves) and the TPC corrections (upper black curves) for target (a) event 1 and (b) event 2. The number of stations contributing to the stack is indicated by the first number below the group label. The lower dashed lines show the Brune-model fit to the corrected spectra (corner frequency in Hertz indicated by the second number below the group label). The upper dashed lines show the fit to the TPC results provided by the model described in the text, characterized by a constant spectrum (red line) and a group-specific value of $\Delta\kappa$ (the number in seconds following the corner frequency). The color version of this figure is available only in the electronic edition.

However, events at greater distances from the target events presumably serve as less accurate EGF events, suggesting there should be a trade-off between using a smaller number of nearby EGF events and a larger number of more distant events (e.g., Abercrombie, 2015; Yoshimitsu *et al.,* 2019). If there are differences in the true TPC between the two target events, potentially due to highly heterogeneous fault structure, then only very nearby EGF events could resolve the path differences.

Both SPAR and SSPEC fit spectra with κ functions, and the variations in the TPCs between the two events at some stations likely result from slightly different best-fitting κ-values. It should be noted that preprocessing choices, such as window length and fitting κ bandwidth, may result in different TPCs for collocated events. For instance, the TPC variation obtained by SPAR at station LRL results from the different high-frequency decay exhibited by the spectra of the two collocated events analyzed in the present study when using a 7 s *S*-wave time window. Using a time window of 5 s, the high-frequency decay of the two event spectra becomes similar, suggesting a bias associated with the choice of time window that could be investigated in future studies. We might also expect each group's station-averaged TPC terms to be the same for the two events, but this is seen only approximately in Figures 5 and 6 because of differences in the stations contributing to each event. This is especially true for methods that

used only a few stations because there are substantial differences in TPCs at different stations for the same event. For example, the ABER results are averaged over four stations for the first target event but averaged over only two stations for the second target event. This causes a much larger difference in the average TPC correction between the two events plotted in Figure 6 than is seen in the TPCs for ABER at specific stations (e.g., stations JRC2 and TEH in Fig. 4).

These results suggest that a large contributing factor to variability in event corner frequencies obtained by different groups arises from disagreement regarding how much the high-frequency part of the raw spectra should be increased to account for path attenuation, including the strong near-surface attenuation that contributes to κ_0 (see the Introduction section).

Figure 7. Corner frequency versus $\Delta\kappa$ estimates for the different methods for (a) P- and (b) S-waves. Values obtained from the fits shown in Figures 5 and 6. The plus symbols and squares indicate the first target event (cuspid 38471103) and second target event (cuspid 38483215), respectively. The color version of this figure is available only in the electronic edition.

Groups that add more high frequencies to their raw spectra will generally obtain higher corner frequencies and stress-drop estimates than groups that add fewer high frequencies. To make this connection more explicit, Figure 7 plots our computed values of corner frequency versus $\Delta\kappa$ for the different methods. Although there is some scatter, there is a strong correlation between f_c and $\Delta\kappa$.

The correlation is clearest for the S-wave results and suggests $\Delta\kappa$ variations from about 0.01–0.04 s, which are roughly associated with an increase in average corner frequency from about 3 to 9 Hz. Note that because f_c is cubed in stress-drop estimation, a threefold change in corner frequency corresponds to a nearly 30 times difference in stress drop. Although this study only examines two earthquakes, systematic differences in the total path correction between groups are a plausible explanation for the offsets seen in the average stress drops for different contributors to the Ridgecrest validation experiment Abercrombie, Baltay, et al. (2024). These offsets are discussed in greater detail elsewhere in this special issue, but Figure 8 shows some systematic shifts in corner frequency for some of the groups contributing to our study. For example, median P-wave corner frequencies for VSF-P are about twice those of TRUG, in rough agreement with the two-event results in Figure 7. Similarly, the S-wave model CHEN has median corner frequencies much higher than BINDI, again consistent with our two-event results.

It is interesting that the range of S-wave $\Delta\kappa$-values seen in Figure 7 is similar to the spread in κ_0-values used to model site attenuation of strong ground motion. For example, Yenier and Atkinson (2014) assumed κ_0-values of 0.0141, 0.0246, and 0.025 s to model the Landers, Northridge, and Parkfield

earthquakes, respectively, and Yenier and Atkinson (2015) simulate ground motions using a range of κ_0-values from 0.01 to 0.04 s chosen to cover values obtained in different site condition studies. Of course, our computed $\Delta\kappa$-values measure differences in the path corrections, whereas κ_0 may also include deviations from the Brune $n = 2$ source model. We have not attempted to compute the path part of κ_0 (hereafter termed path κ_0) for the different groups, which would require estimating the range-independent part of the TPC from the different stations and would be best performed using many more stations than those analyzed here. But our results suggest that much of the variation in $\Delta\kappa$ we observe among the groups may arise from differences in path κ_0, reflecting the tradeoff between deviations from the Brune source model and shallow crustal attenuation.

Obtaining accurate stress drops remains an important goal in seismology, both to inform our understanding of earthquake rupture dynamics and to quantify how much the observed variability of ground motions is related to source differences compared to path effects. The Ridgecrest stress-drop validation study by Baltay et al. (2024) and Abercrombie, Baltay, et al. (2024) has shown that different groups obtain very different stress-drop results for the same earthquakes. This could be caused by many factors, including event selection criteria, signal-to-noise cutoffs, details of fitting spectra with models, and

Figure 8. Corner frequency versus magnitude as obtained by different methods for the Ridgecrest test earthquakes for (a) *P*- and (b) *S*-waves. The plus symbols and squares indicate the first and second target events, respectively. Other events are shown as small dots. The curves trace median values in 0.5 magnitude bins for cases where at least five bin values are available. Note that the target event corner frequencies plotted do not necessarily match the values plotted in Figure 7 because they were computed by the individual groups using their own fitting procedures. The color version of this figure is available only in the electronic edition.

conversion from corner frequency to stress drop. A primary goal of our study was to examine how much differences in assumed source–receiver path corrections may be contributing to stress-drop disagreements. To simplify the problem, we select two target M ~3 earthquakes recorded at a small number of stations, so that we could examine results for single spectra prior to any stacking. Our results document wide variations in the path corrections that different groups apply and indicate this is likely a major contributor to stress-drop uncertainty.

Each of the methods described here likely has advantages and disadvantages and may work better for some data sets than others. However, all the approaches estimate path corrections (either explicitly or implicitly) by fitting spectral data with models, and they presumably obtain reasonable fits to their data (excepting the possibility of computer bugs). Thus, it seems likely that the accuracy of the path correction estimates is not well determined by the quality of the data fits, there is no unique solution to fitting the spectral data, and that corner-frequency uncertainty estimates based solely on data misfit criteria will underestimate the true uncertainties. This is consistent with an analysis of over 3000 Landers aftershocks by Shearer et al. (2019), who compared the spectral decomposition and spectral ratio approaches and found that both methods have too many parameter trade-offs to reliably separate path and source effects.

Thus, although it may be possible in principle to separate path and source effects, this may require ideal conditions that are not met with typical earthquake data sets. Two factors are particularly important. First, much of the path attenuation occurs at shallow depths below the stations, causing a range-independent depletion in high frequencies that is hard to distinguish from source effects (i.e., changes in earthquake corner frequency or high-frequency fall-off rate). Because some of this shallow attenuation is common to all stations, it is not averaged out in large-scale analyses, as might occur for other site-response effects, such as layer resonances. Second, spectra from real earthquakes are generally somewhat irregular in appearance, that is, they rarely resemble the smooth Brune or Boatwright models often assumed in the modeling. This further limits the ability of best-fitting models to distinguish between source and path effects.

Given these considerations, attempting to determine which of the methods presented here gives the "best" answer is not possible without additional information. Accurate path corrections are critical to obtaining unbiased source spectral estimates, but the wide variability in path corrections among different groups suggests that traditional empirical approaches are failing to obtain reliable path corrections. Studying how the path differences among the groups relate to specific details of their methods is important, as it may lead to improved

methods (a goal of the stress-drop validation exercise), but is beyond the scope of this study.

What can the seismology community do to address these issues? Here are some ideas:

1. Recognize that there are likely large uncertainties in path correction estimates, even when fits to the data appear good, and attempt to devise measures to compare average path terms with those of other groups. One possibility would be to estimate and publish path κ_0-values along with corner frequencies and stress drops, which would make it easier to examine path-dependent differences between studies, make results more reproducible, and strengthen connections to strong ground motion modeling. The best approach to computing path κ_0 will vary among the different spectral analysis methods, but in principle can always be obtained by examining the TPC term versus range and fitting an exponential function to its range-independent component.

2. Focus less on absolute source spectral estimates (and inferred stress drops) and more on relative differences in source properties using methods that enforce similar path corrections for nearby events. There are real differences in the high-frequency radiation among sources that can be explored even without knowing the true path correction or absolute source spectral shape.

3. Fix the average corner frequencies of small reference earthquakes in the data set rather than attempting to estimate them empirically (e.g., Shearer et al., 2022; Ruhl et al., 2023). This effectively sets the average stress drop of the reference earthquakes and dampens any true spatial variations in stress drop. However, it has the great advantage of ensuring that any observed spatial variations in stress drop are real and not an artifact of inaccurate path corrections. This approach was used for the VSF-P and VSF-S models, which are described in greater detail in Vandevert et al. (2024). Although this idea has been applied mostly to the spectral decomposition method, it could easily be adopted to other methods as well. For example, the corner frequencies of the smaller events in the spectral ratio approach could be fixed, which would help stabilize the method (see discussion in Shearer et al., 2019) and ensure greater self-consistency in the effective TPC for near by target events.

4. Assume or solve for a seismic velocity and attenuation model and compute and apply path corrections consistent with the model. This has the advantage of ensuring that path corrections are physically plausible, which is not the case for purely empirical approaches such as spectral decomposition and spectral ratios. Because the attenuation model parameters would be provided along with any source parameters, this would also facilitate path-adjusted comparisons among groups. However, it is not yet clear whether the key shallow part of attenuation models (related to κ_0) can be reliably determined without borehole data.

DATA AND RESOURCES

DECLARATION OF COMPETING INTERESTS

ACKNOWLEDGMENTS

REFERENCES

Abercrombie, R. E. (1997). Near-surface attenuation and site effects from comparison of surface and deep borehole recordings, *Bull. Seismol. Soc. Am.* **87**, no. 3, 731–744.

Abercrombie, R. E. (2014). Stress drops of repeating earthquakes on the San Andreas fault at Parkfield, *Geophys. Res. Lett.* **41**, no. 24, 8784–8791.

Abercrombie, R. E. (2015). Investigating uncertainties in empirical Green's function analysis of earthquake source parameters, *J. Geophys. Res.* **120**, no. 6, 4263–4277.

Abercrombie, R. E. (2021). Resolution and uncertainties in estimates of earthquake stress drop and energy release, *Phil. Trans. Roy. Soc. Lond. A* **379**, no. 6, doi: 10.1098/rsta.2020.0131.

Abercrombie, R. E., and P. Leary (1993). Source parameters of small earthquakes recorded at 2.5 km depth, Cajon Pass, southern California: implications for earthquake scaling, *Geophys. Res. Lett.* **20**, no. 14, 1511–1514.

Abercrombie, R. E., A. Baltay, S. Chu, T. Taira, D. Bindi, O. Boyd, X. Chen, E. Cochran, E. Devin, D. Dreger, et al. (2024). Overview of the SCEC/USGS community stress drop validation study using the 2019 Ridgecrest earthquake sequence, *Bull. Seismol. Soc. Am.* (under revision).

Abercrombie, R. E., S. Bannister, J. Ristau, and D. Doser (2017). Variability of earthquake stress drop in a subduction setting, the Hikurangi Margin, New Zealand, *Geophys. J. Int.* **208**, 306–320.

Abercrombie, R. E., X. Chen, Y. Huang, and S. Chu (2024). Comparison of EGF methods for Ridgecrest Sequence: Can EGF be used to help resolve ambiguity in isolating source spectra? *Bull. Seismol. Soc. Am.* (under revision).

Aki, K. (1967). Scaling law of seismic spectrum, *J. Geophys. Res.* **72**, no. 4, 1217–1231.

Anderson, J. G. (1986). Implication of attenuation for studies of the earthquake source, in *Earthquake Source Mechanics*, S. Das, J. Boatwright, and C. Scholz (Editors), Vol. 37, 311–318.

Anderson, J. G., and S. E. Hough (1984). A model for the shape of the Fourier amplitude spectrum of acceleration at high frequencies, *Bull. Seismol. Soc. Am.* **74,** no. 5, 1969–1993.

Aster, R. C., and P. M. Shearer (1991). High-frequency borehole seismograms recorded in the San Jacinto Fault zone, Southern California Part 2. Attenuation and site effects, *Bull. Seismol. Soc. Am.* **81,** no. 4, 1081–1100.

Baltay, A., and R. E. Abercrombie (2024). Southern California moment and magnitude scales from the SCEC/USGS community stress drop validation study, *Bull. Seismol. Soc. Am.* (under revision).

Baltay, A., R. Abercrombie, S. Chu, and T. Taira (2024). The SCEC/USGS community stress drop validation study using the 2019 Ridgecrest earthquake sequence, *Seismica* **3,** no. 1, doi: 10.26443/seismica.v3i1.1009.

Bindi, D., D. Spallarossa, M. Picozzi, A. Oth, P. Morasca, and K. Mayeda (2023a). The community stress-drop validation study-part I: Source, propagation, and site decomposition of Fourier spectra, *Seismol. Res. Lett.* **94,** no. 4, 1980–1991.

Bindi, D., D. Spallarossa, M. Picozzi, A. Oth, P. Morasca, and K. Mayeda (2023b). The community stress-drop validation study-part II: Uncertainties of the source parameters and stress drop analysis, *Seismol. Res. Lett.* **94,** no. 4, 1992–2002.

Bindi, D., D. Spallarossa, M. Picozzi, A. Oth, P. Morasca, and K. Mayeda (2023c). Spectral decomposition results for the SCEC-community stress drop validation study, *GFZ Data Services*, doi: 10.5880/GFZ.2.6.2023.005.

Brune, J. N. (1970). Tectonic stress and the spectra of seismic shear waves from earthquakes, *J. Geophys. Res.* **75,** no. 26, 4997–5009.

Calderoni, G., and R. E. Abercrombie (2023). Investigating spectral estimates of stress drop for small to moderate earthquakes with heterogeneous slip distribution: Examples from the 2016–2017 Amatrice earthquake sequence, *J. Geophys. Res.* **128,** no. 6, e2022JB025022, doi: 10.1029/2022JB025022.

Calderoni, G., A. Rovelli, and R. Di Giovambattista (2019). Stress drop, apparent stress, and radiation efficiency of clustered earthquakes in the nucleation volume of the 6 April 2009, M_w 6.1 L'Aquila earthquake, *J. Geophys. Res.* **124,** no. 10, 10,360–10,375.

Chen, X., and R. Abercrombie (2020). Improved approach for stress drop estimation and its application to an induced earthquake sequence in Oklahoma, *Geophys. J. Int.* **223,** no. 1, 233–253.

Chen, X., Q. Wu, and C. Pennington (2024). Influence factors of variability in stress drop measurements using stacking and spectral ratio methods for the Ridgecrest sequence, *Bull. Seismol. Soc. Am.* (under revision).

Cochran, E. S., A. Baltay, S. Chu, R. E. Abercrombie, D. Bindi, X. Chen, G. A. Parker, C. Pennington, P. M. Shearer, and D. T. Trugman (2024). SCEC/USGS community stress drop validation study: How spectral fitting approaches influence measured source parameters, *Bull. Seismol. Soc. Am.* doi: 10.1785/0120240140.

Frankel, A. (1982). The effects of attenuation and site response on the spectra of microearthquakes in the northeastern Caribbean, *Bull. Seismol. Soc. Am.* **72,** no. 4, 1379–1402.

Hanks, T. C. (1982). f max. *Bull. Seismol. Soc. Am.* **72,** no. 6A, 1867–1879.

Hanks, T. C., and R. K. McGuire (1981). The character of high-frequency strong ground motion, *Bull. Seismol. Soc. Am.* **71,** no. 6, 2071–2095.

Huang, Y., G. C. Beroza, and W. L. Ellsworth (2016). Stress drop estimates of potentially induced earthquakes in the Guy-Greenbrier sequence, *J. Geophys. Res.* **121,** no. 9, 6597–6607.

Huang, Y., W. L. Ellsworth, and G. C. Beroza (2017). Stress drops of induced and tectonic earthquakes in the central United States are indistinguishable, *Sci. Adv.* **3,** no. 8, e1700772, doi: 10.1126/sciadv.1700772.

Kemna, K. B., A. Verdecchia, and R. M. Harrington (2021). Spatio-temporal evolution of earthquake static stress drop values in the 2016–2017 central Italy seismic sequence, *J. Geophys. Res.* **126,** no. 11, e2021JB022566, doi: 10.1029/2021JB022566.

Knudson, T. C., W. L. Ellsworth, and G. C. Beroza (2024). Source parameter analysis using maximum amplitudes in the time domain, *Bull. Seismol. Soc. Am.* (under revision).

Liu, M., Y. Huang, and J. Ritsema (2020). Stress drop variation of deep-focus earthquakes based on empirical Green's functions, *Geophys. Res. Lett.* **47,** no. 9, e2019GL086055, doi: 10.1029/2019GL086055.

Mori, J., and A. Frankel (1990). Source parameters for small events associated with the 1986 North Palm Springs, California, earthquake determined using empirical Green functions, *Bull. Seismol. Soc. Am.* **80,** no. 2, 278–295.

Mueller, C. S. (1985). Source pulse enhancement by deconvolution of an empirical Green's function, *Geophys. Res. Lett.* **12,** no. 1, 33–36.

Pennington, C. N., X. Chen, R. E. Abercrombie, and Q. Wu (2021). Cross validation of stress drop estimates and interpretations for the 2011 Prague, OK, earthquake sequence using multiple methods, *J. Geophys. Res.* **126,** e2020JB020888, doi: 10.1029/2020JB020888.

Ruhl, C. J., R. E. Abercrombie, and P. M. Shearer (2023). Spatially consistent small-scale stress heterogeneity revealed by the 2008 Mogul, Nevada, earthquakes, *Seism. Rec.* **3,** no. 3, 239–248.

Satriano, C. (2022). SourceSpec–Earthquake source parameters from P- or S-wave displacement spectra (v1.6), *Zenodo*, doi: 10.5281/zenodo.6954238.

Shearer, P. M., R. E. Abercrombie, and D. T. Trugman (2022). Improved stress drop estimates for M 1.5 to 4 earthquakes in southern California from 1996 to 2019, *J. Geophys. Res.* **127,** no. 7, e2022JB024243, doi: 10.1029/2022JB024243.

Shearer, P. M., R. E. Abercrombie, D. T. Trugman, and W. Wang (2019). Comparing EGF methods for estimating corner frequency and stress drop from P wave spectra, *J. Geophys. Res.* **124,** no. 4, 3966–3986.

Shearer, P. M., G. A. Prieto, and E. Hauksson (2006). Comprehensive analysis of earthquake source spectra in southern California, *J. Geophys. Res.* **111,** no. B6, doi: 10.1029/2005JB003979.

Supino, M., G. Festa, and A. Zollo (2019). A probabilistic method for the estimation of earthquake source parameters from spectral inversion: application to the 2016-2017 central Italy seismic sequence, *Geophys. J. Int.* **218,** no. 2, 988–1007.

Supino, M., L. Scognamiglio, L. Chiaraluce, C. Doglioni, and A. Herrero (2024). Source characterization of the 20th May 2024 MD 4.4 Campi Flegrei caldera earthquake through a joint source-propagation probabilistic inversion, *Seismica* **3,** no. 2, doi: 10.26443/seismica.v3i2.1394.

Trugman, D. T. (2020). Stress-drop and source scaling of the 2019 Ridgecrest, California, earthquake sequence, *Bull. Seismol. Soc. Am.* **110,** no. 4, 1859–1871.

Trugman, D. T., and P. M. Shearer (2017). Application of an improved spectral decomposition method to examine earthquake source scaling in Southern California, *J. Geophys. Res.* **122,** no. 4, 2890–2910.

Vandevert, I. C., P. M. Shearer, and W. Fan (2024). Ridgecrest aftershock stress drops from P- and S-wave spectral decomposition, *Bull. Seismol. Soc. Am.* doi: 10.1785/0120240133.

Yenier, E., and G. M. Atkinson (2014). Equivalent point-source modeling of moderate-to-large magnitude earthquakes and associated ground-motion saturation effects, *Bull. Seismol. Soc. Am.* **104,** no. 3, 1458–1478.

Yenier, E., and G. M. Atkinson (2015). Regionally adjustable generic ground-motion prediction equation based on equivalent point-source simulations: Application to central and eastern North America, *Bull. Seismol. Soc. Am.* **105,** no. 4, 1989–2009.

Yoshimitsu, N., W. L. Ellsworth, and G. C. Beroza (2019). Robust stress drop estimates of potentially induced earthquakes in Oklahoma: Evaluation of empirical Green's function, *J. Geophys. Res.* **124,** no. 6, 5854–5866.

Zhang, J., and H. Yang (2024). Improved source parameter estimation of earthquakes in the 2019 Ridgecrest Sequence based on a global-optimization algorithm and their implications on fault behaviors, *Bull. Seismol. Soc. Am.* (under revision).

Zhang, J., H. Yang, J. Zi, J. Su, and X. Chen (2024). An improved estimation of stress drop and its application on induced earthquakes in the Weiyuan Shale Gas Field in China, *Geophys. J. Int.* **236,** no. 3, 1785–1803.

APPENDIX: METHOD DESCRIPTIONS

This section provides brief descriptions of each of the spectral analysis methods compared in this study.

Abercrombie (model ABER)

This method applies the stacked empirical Green's function (EGF) spectral ratio approach to S-wave records by Abercrombie (2014), Abercrombie et al. (2017), Pennington et al. (2021), also see Abercrombie, Chen, et al. (2024).

Bindi (model BINDI)

This method uses the spectral decomposition approach of Bindi et al. (2023a) to isolate the source spectra from propagation and site effects. With respect to the logic-tree structure used by Bindi et al. (2023b), here we consider the solutions obtained for S-wave windows of 20 s (model 20), using the hypocentral attenuation model (model HYPO) and a priori constraining the average amplification of a selected subset of stations (model SEL). The results are available in Bindi et al. (2023c).

Calderoni (model CALD-S)

We estimate the Brune stress drop following spectral fitting analysis as described in Calderoni et al. (2019) and Calderoni and Abercrombie (2023). The method fits individual spectra for κ to account for attenuation, using station-specific κ terms

computed from 8 $M_w \geq 3.5$ earthquakes to account for station site effects in producing the final source spectral estimates.

Chen (model CHEN)

This method computes the S-wave displacement spectra from the geometrical mean of the two horizontal channels, then applies spectral decomposition (e.g., Shearer et al., 2006) to S waves for the entire Ridgecrest data set to obtain event terms. To obtain stress drop, we assume a fixed stress drop of the M 1.5 magnitude bin and follow Chen and Abercrombie (2020) to estimate an empirical correction spectrum (ECS) using all the available events in the study region ("constant-ECS"). More details are included in Chen et al. (2024).

Huang (model HUANG)

This method computes P-wave spectral ratios following the methods described by Huang et al. (2016, 2017) and Liu et al. (2020). We use three EGF events for target event 38471103 and two EGF events for target event 38483215 with all EGF events within 250 m from the target events. Note that fewer EGF events are used here than in the community validation study, due to low signal-to-noise ratios for other EGF events at the subset of stations considered in this study.

Knudson (model KNUD)

This method by Knudson et al. (2024) computes S-wave spectra from the peak amplitude of narrow band-pass-filtered seismograms and then applies empirical corrections for frequency-dependent attenuation functions derived from a subset of the events.

Rossbach (models ROSS-P and ROSS-S)

The method applies the approach of Kemna et al. (2021) to P- and S-wave spectra. Using a large data set of ~5.3 million individual station spectra, a grid search is performed to find best-fitting values for Q and n. The Q-value is then used to correct individual station spectra for each event, which are then stacked to obtain station-averaged source spectral estimates.

Satriano (model SSPEC)

This method applies SourceSpec (v.1.8, Satriano, 2022) to S-wave spectra, which first fits each individual spectrum separately for Ω_0 and κ, assuming a Brune ($n = 2$) source model. Then mean station residuals are computed by averaging the event results and used to correct the measured spectra in a second run of SourceSpec.

Supino (model SPAR)

This method applies the probabilistic approach described by Supino et al. (2019) to each individual S-wave spectra to solve for an high-frequency (HF) source fall-off rate n and an attenuation term that accounts for both Q and κ_0 in Supino et al. (2024). Site-effect terms are then computed from the residuals, and the

final source spectrum estimate for each earthquake is the average of the path-specific and site-term corrected station spectra.

Trugman (model TRUG)

This method applies spectral decomposition and ECS estimation to *P* waves using the approach of Trugman and Shearer (2017). Details are in Trugman (2020), which describes one of the first data sets of source spectral parameter estimates for the Ridgecrest sequence.

Vandevert, Shearer, and Fan (models VSF-P and VSF-S)

This method applies the spectral decomposition method (e.g., Shearer *et al.*, 2006; Trugman and Shearer, 2017), as recently modified by Shearer *et al.* (2022) to directly set the average corner frequency of the small calibration events in the data set when estimating the ECS. More details are in Vandevert *et al.* (2024), which describes how some of the *S*-wave parameters were set to obtain rough agreement between the *P*- and *S*-wave results.

Zhang (models ZHANG-P and ZHANG-S)

This method applies an approach based on spectral decomposition termed "Differential-Evolution-based Spectral Correction" (DESC), which is described in Zhang *et al.* (2024). The *P* and *S* spectra are analyzed independently. Specific details for the Ridgecrest data set are provided in Zhang and Yang (2024).